New Journal of Physics
The open access journal at the forefront of physics

Deutsche Physikalische Gesellschaft DPG
IOP Institute of Physics

Published in partnership with: Deutsche Physikalische Gesellschaft and the Institute of Physics

OPEN ACCESS

RECEIVED
9 October 2019

REVISED
21 December 2019

ACCEPTED FOR PUBLICATION
16 January 2020

PUBLISHED
4 February 2020

PAPER

Achromatic reflected metalens for highly directional and long-distance acoustic probing

Peifeng Wang[1], **Gaokun Yu**[1], **Yong Li**[2], **Xinlong Wang**[3] **and Ning Wang**[1]

[1] College of Information Science and Engineering, Ocean University of China, Qingdao 266100, People's Republic of China
[2] Institute of Acoustics, School of Physics Science and Engineering, Tongji University, 200092 Shanghai, People's Republic of China
[3] Key Laboratory of Modern Acoustics and Institute of Acoustics, Nanjing University, Nanjing 210093, People's Republic of China

E-mail: gkyu@ouc.edu.cn

Keywords: achromatic metalens, highly directional acoustic probing, hybrid resonance, anti-resonance

Abstract

Simultaneous temporal and spatial focusing of a pulse is of significance for detection and imaging. Here, an achromatic reflected metalens is designed using hybrid resonance and anti-resonance. The theoretical result demonstrates that the anti-resonance provides an extra degree of freedom to control local phases of reflected waves, yielding an achromatic lens of thickness equal to one half of central wavelength. To overcome the shortcoming of traditional approach to design lenses (neglecting the intercell coupling), a boundary integral method is proposed to alleviate the focus deviation over a broadband. The achromatic feature of designed lens is then verified in the frequency range from 2800 to 5600 Hz by an experiment. Owing to a very weak frequency dependence of focal point and a high reflected focusing efficiency over a broadband, a highly directional and long-distance acoustic probing scheme (the mainlobe width about 8^0) is proposed with the aid of achromatic reflected metalens and being confirmed by another experiment, where a signal processing method using triple sensors separated by a subwavelength interval is adopted to eliminate the interferences between incident waves and reflected waves. Our result may find its application in a long-distance underwater acoustic probing.

1. Introduction

Owing to the development of metamaterials and metasurfaces, optical focusing and imaging by lenses have attracted much attention from scientists, such as a perfect lens for subwavelength imaging [1] and achromatic metalenses for full-color detection and imaging [2–5]. Advances in optical focusing and imaging have inspired researchers in acoustics to design novel acoustic focusing and imaging devices. Various kinds of acoustic lenses have been designed for focusing of transmitted waves, such as GRIN (gradient index) sonic lenses [6, 7], GRIN lenses using cross-shaped scatterers [8], coiled up space [9–11], rigid toroidal scatterers [12] and orifice-type metamaterial [13, 14], acoustic Fresnel lenses [15–18], planar diffractive acoustic lenses [19–22]. Most of the above works focused on designing ultra-thin lenses [8, 10, 11, 16–22], resulting in the focal length highly dependent on frequency due to the refractive index (or the properties of diffractive elements) sensitive to frequency, whereas the GRIN lenses using orifice-type metamaterial [13, 14] demonstrated near-frequency-independent characteristics, with its thickness being on the order of wavelength. Different from GRIN lenses, which rely on gradually varying refractive index to obtain phase delay, diffractive lenses are realized by controlling local phases of transmitted waves to generate interference and diffraction patterns. The concept of local phase is also used to achieve the focusing of reflected waves [23–28], such as reflected lenses using Fano resonance [26, 27] and Helmholtz resonance [28]. Usually, the focal length also has dependence on frequency, and thus there are few works on acoustic achromatic focusing. Although a dispersionless manipulation of reflected acoustic wavefront [23] was proposed to achieve acoustic achromatic focusing, the thickness of lens was on the order of wavelength. Since simultaneous temporal and spatial focusing of a pulse by an acoustic achromatic lens is advantageous in ultrasound therapy and long-distance acoustic probings (an example

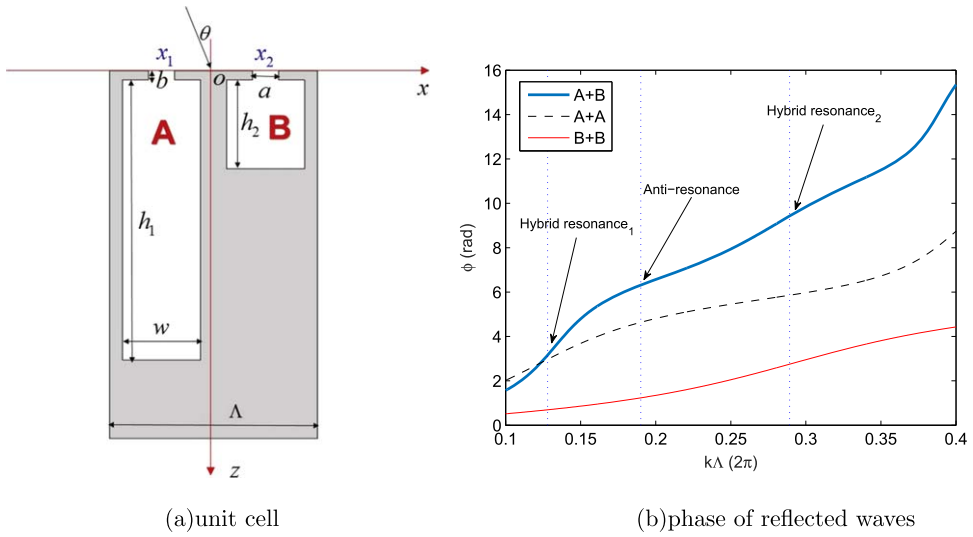

Figure 1. (a) A unit cell consisting of two coupled Helmholtz resonators A and B with different cavity heights h_1 and h_2, respectively. Corresponding dimensions of resonator: the size of throat $a = 0.125\Lambda$, the length of throat $b = 0.05\Lambda$, the width of cavity $w = 0.375\Lambda$, and the height of cavity $h_1 = 1.522\ 5\Lambda$ and $h_2 = 0.484\ 2\Lambda$, where Λ denotes the length of unit cell. (b) The phase of reflected waves for a sound wave normally incident on a metasurface, with each unit cell being constructed by a combination of two resonators. In addition, hybrid resonance and anti-resonance for two coupled resonators A and B are marked by dotted lines.

investigated in this paper), it is necessary to seek an effective physical mechanism to control phases of reflected waves, and thus reducing the thickness of achromatic lens.

On the other hand, hybrid resonance, which originates from couplings between two different resonances, was proposed to achieve acoustic absorption [29–33], broadband acoustic energy harvesting [34], and broadband blazed acoustic gratings [35]. It is well known that hybrid resonance is always accompanied by anti-resonance, which has been used to achieve negative dynamic mass [36], sound-proof metamaterial [37], acoustic transparency [38–40], and acoustics metasurface carpets [41].

Usually, anti-resonance [29, 36] was used to describe the zero average displacement of a vibrating membrane, resulting in high transmission loss. Here, the concept of anti-resonance is extended to the case of pure-reflection metasurface. By analyzing the property of hybrid resonance and anti-resonance, we find that anti-resonance as well as hybrid resonance can be utilized to manipulate the local phase ϕ of reflected wave, where ϕ is zero (or 2π) at anti-resonance and ϕ is π at hybrid resonance. Therefore, we first design an achromatic reflected metalens with its thickness being equal to one half of central wavelength, using hybrid resonance and anti-resonance induced by couplings between two Helmholtz resonators. By considering couplings among different cells, an improved design based on the boundary integral method is obtained. Second, a highly directional and long-distance acoustic probing scheme is proposed by a combination of achromatic reflected metalens and triple sensors separated by a subwavelength interval, in which a signal processing method is adopted to eliminate interferences between incident waves and reflected waves, resulting in a highly directional receiving pattern. Note that the mechanism of our acoustic probing scheme is totally different from the highly directive-sensitive detection by an acoustic metamaterial with a near-zero-index [42].

2. Hybrid resonance and anti-resonance

By couplings between two different Helmholtz resonators (see in figure 1(a)), hybrid resonance and anti-resonance are adopted to obtain the local phase of reflected waves. Figure 1(b) shows the phase for a sound wave normally incident on a metasurface, which is extracted from the reflection coefficient, given in appendix A. For a metasurface with each unit cell being constructed by two different resonators 'A+B', the phase-frequency curve lies above that of two identical resonators 'A+A'(or 'B+B') due to an anti-resonance located between two different hybrid resonances, which is investigated in appendix B and being marked in figure 1(b). The phase of reflected waves at the anti-resonance point ($f = 0.19c_0/\Lambda$) is 2π, but for a metasurface constructed by identical resonators, a 2π phase is obtained at a higher frequency, for example, $f = 0.324\ 8c_0/\Lambda$ for 'A+A', which means the thickness of lens can be reduced by the adoption of anti-resonance. By tuning resonant frequencies of resonator A and B, i.e. tuning the anti-resonance point, the slope of phase-frequency curve can be approximated as a constant over a broadband as shown in figure 1(b), which is used to design an achromatic metalens. In

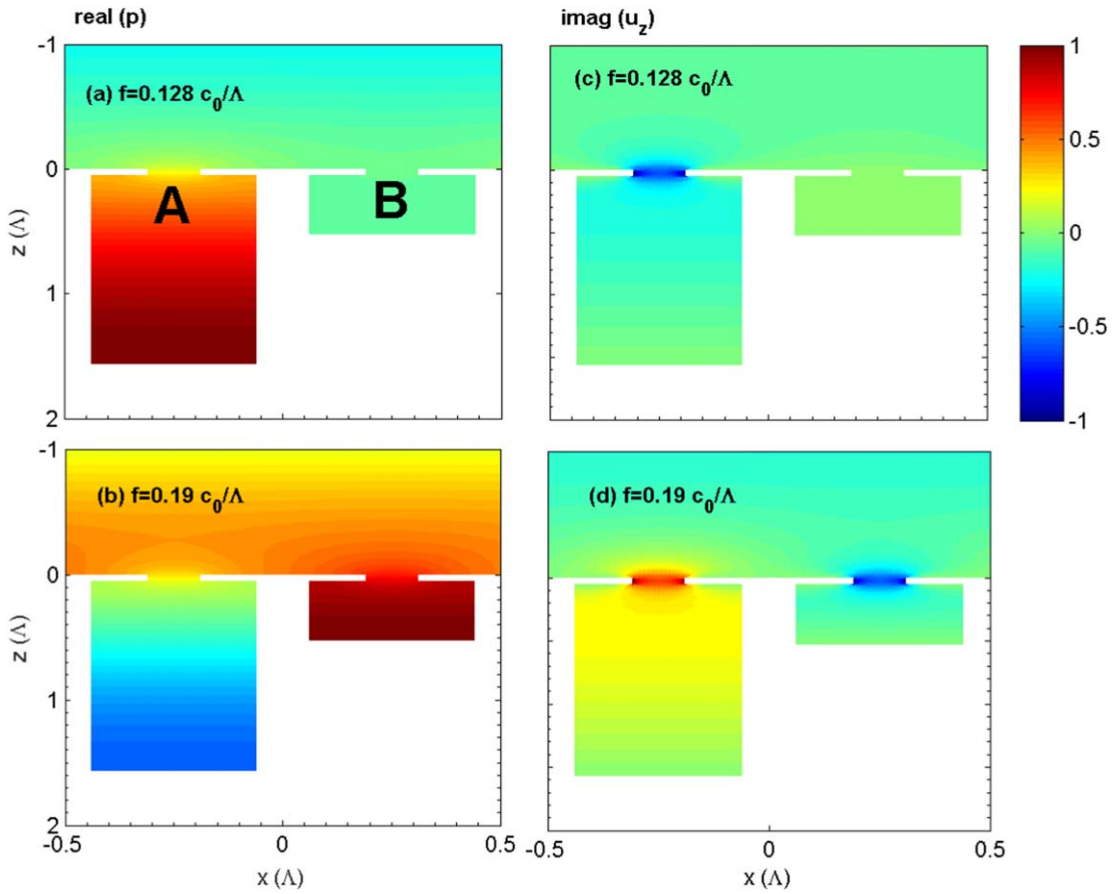

Figure 2. Distributions of sound pressure p and normal velocity u_z. (a) and (c) represent distributions of real part of pressure p and imaginary part of normal velocity u_z at frequency of hybrid resonance $f = 0.128c_0/\Lambda$, whereas (b) and (d) represent distributions at frequency of anti-resonance $f = 0.19c_0/\Lambda$. Note that parameters are the same as that for figure 1.

addition, hybrid resonance$_1$ and hybrid resonance$_2$ marked in figure 1(b) are at frequencies near resonances of resonator A and resonator B, respectively.

It is illustrated in figures 2(a) and (c) the distributions of sound pressure p and normal velocity u_z at frequency of hybrid resonance $f = 0.128c_0/\Lambda$, where only resonator A vibrates strongly. However, the anti-resonance leads to sound pressures being out of phase in two different cavities (see in figure 2(b)). By the discuss in appendix B, an anti-resonance occurs when the total volume velocity over a unit cell is zero. It is shown in figure 2(d) the distribution of normal velocity u_z at frequency of anti-resonance $f = 0.19c_0/\Lambda$, where air vibrations at the inlets of two Helmholtz resonators are out of phase, and the average velocity over a unit cell is zero.

3. The design of achromatic metalens and experimental confirmation

For an achromatic reflected metalens (see in figure 3(a)), the local phases of reflected waves for the nth unit cell and the first unit cell, ϕ_n and ϕ_1, follow a simple relation

$$\phi_n + k\sqrt{x_{cn}^2 + f_0^2} = \phi_1 + k\sqrt{x_{c1}^2 + f_0^2}, \tag{1}$$

where f_0 is the focal length, x_{cn} is the center position of the nth unit cell, $k = \omega/c_0$ is the wavenumber. The reflected phase ϕ_n of the nth unit cell, represents the phase retardation due to the sound propagation inside resonators, while the term $k\sqrt{x_{cn}^2 + f_0^2}$ represents the phase retardation due to the sound propagation from the center position of the nth unit cell to the focal point, therefore, the left-hand side of equation (1) represents that the phase retardation between the wave generated by the nth unit cell and the normally incident plane wave. And the equality constraint in equation (1) means the same phase retardation for each unit cell, resulting the acoustic focusing by the constructive interference. It is also seen from equation (1) that if the phase difference $\phi_n - \phi_1$ has a linear dependence on frequency, then the focal length has no dependence on frequency. Although the reflected phase ϕ_n can be a function of frequency with arbitrary dependence, an approximate linear dependence on frequency is chosen in the range of frequencies of interest. This is because that the reflected phase at the edge

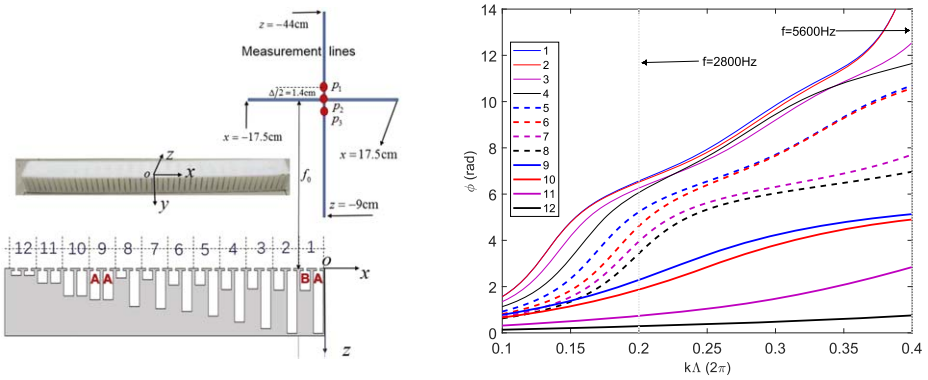

(a)Experimental scheme of achromatic focusing (b)phases for 12 different unit cells

Figure 3. (a) A photo of 3D printed metalens and the detailed distribution of 12 unit cells for half of metalens due to symmetry, where the size of throat $a = 0.125\Lambda$, the length of throat $b = 0.05\Lambda$, the width of cavity $w = 0.375\Lambda$ are fixed. Note that for a plane wave normally incident on metalens, the focal length f_0 is 10Λ, three times the central wavelength at frequency $f = 4200$ Hz. (b) Dependence of phases of reflected waves on frequency, where the number (1, 2, ⋯, 12) in legend corresponds to unit cells marked in (a).

Table 1. The cavity heights h_1 and h_2 for 12 unit cells.

Unit cell	1	2	3	4	5	6	7	8	9	10	11	12
$h_1(\Lambda)$	1.5225	1.5223	1.4043	1.2487	1.1030	0.9927	0.9264	0.8680	0.7079	0.6131	0.3010	0.1241
$h_2(\Lambda)$	0.4842	0.4725	0.4430	0.4606	0.3513	0.3499	0.2185	0.1776	0.7079	0.6131	0.3010	0.1241

of metalens is smaller than that near the center, and if the reflected phase at the edge is set to zero, the reflected phase ϕ_1 near the center determined by equation (1) has a linear dependence on frequency. Note that the linear frequency dependence is difficult to achieve, therefore, an optimizing procedure is adopted to design the metalens with a constraint that the reflected phase is an approximate linear dependence function of frequency.

A metalens is initially designed from equation (1) and then optimized by maximizing the following objective function J

$$J = \sum_f \exp\left(-\frac{2\pi f\sqrt{(x_{\max}-x_0)^2+(y_{\max}-y_0)^2}}{\gamma c_0}\right)\frac{|p_s(x_0,y_0)|^2}{\frac{1}{S}\iint_s |p_s(x,y)|^2 \mathrm{d}S}, \tag{2}$$

where the scattered pressure $|p_s(x, y)|$ is obtained by the boundary integral method in appendix C, (x_0, y_0) is a predetermined position of focus, $(x_{\max}, y_{\max})$ is a position of maximum $|p_s(x, y)|$, and S denotes a zone in which the scattered pressure is calculated. The term $S\,|p_s(x_0, y_0)|^2 \Big/ \iint_s |p_s(x, y)|^2 \mathrm{d}S$ suppresses unwanted side-lobes in the zone S, whereas the exponential term in equation (2) plays a role to reduce focus deviation over a broad frequency band. For a large value of γ, the value of exponential term changes slowly when the focusing position deviates from the predetermined position, and thus the ability to reduce focus deviation is weak. For a small value of γ, the ability to reduce focus deviation is enhanced, however, the unwanted side-lobes may appear due to the exponential term dominating the objective function in this situation. After several attempts, the value of γ is then set to 2 in simulation. A particle swarm optimization algorithm is adopted to obtain the best parameters with 21 discrete frequency points in the range from 2800 to 5600 Hz.

The corresponding optimized cavity heights h_1 and h_2 for each unit cell are listed in table 1. For unit cells numbered from 1 to 8 are constructed by two different Helmholtz resonators, marked by A and B in figure 3(a), whereas for unit cells numbered from 9 to 12 are constructed by two identical Helmholtz resonators, marked by A and A. The phase-frequency curves for 12 unit cells are illustrated in figure 3(b), where the large phase retardation near the center of metalens and the small phase retardation near the edge of metalens are obtained to compensate geometrical acoustical path difference over a broad frequency band. It is noted that this distribution of unit cells is not a direct result from the optimization procedure by the boundary integral method. Since the existence of anti-resonance induced by two different resonators provides the larger phase retardation than that of two identical resonators as shown in figure 1(b), we choose the unit cells of different resonators near the center and the unit cells of identical resonators near the edge. More specifically, the cavity height of the 12th unit cell is chosen with the predetermined small value, and from the reflected coefficient we obtain the local phase ϕ_{12}, which is then substituted into equation (1) to get a reference curve of reflected phase for the first unit cell $\phi_{1\mathrm{ref}}$.

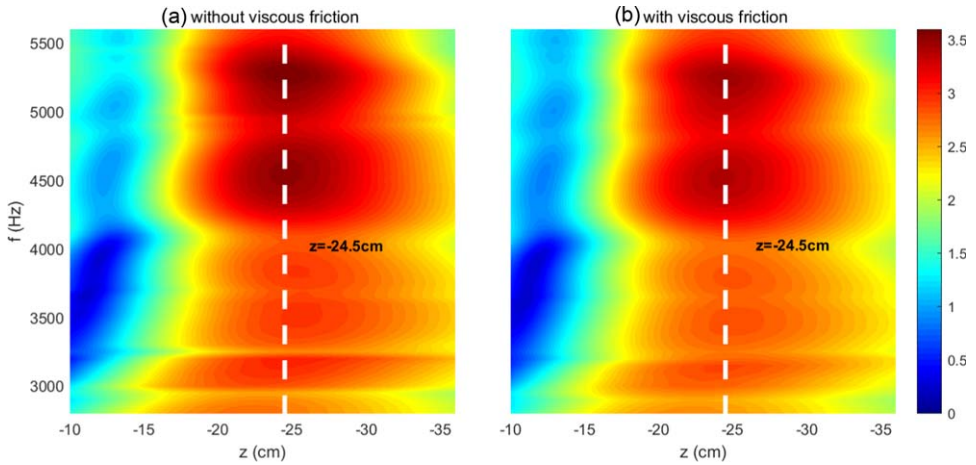

Figure 4. Frequency dependence of scattered amplitude $|p_s(x,\ z)|$ along $x = 0$ cm for a normally incident plane wave of unit amplitude. (a) For the simulated result without considering the viscous friction due to the existence of narrow channels, and (b) for the result with viscous friction. Note that the predetermined focusing position is (0, −24.5 cm) for a normally incident plane wave.

Note that $\phi_{1\mathrm{ref}}$ in the range of frequencies of interest is an approximate linear dependence function of frequency. By minimizing the objective function $|\exp(i\phi_1) - \exp(i\phi_{1\mathrm{ref}})|$ using a particle swarm optimization algorithm, we obtain optimized cavity heights of the first unit cell, then the optimized cavity heights of the nth unit cell is obtained by minimizing the objective function $|\exp(i\phi_n) - \exp(i\phi_1)|$. The above optimization procedure leads to a distribution of the optimized cavity heights, i.e. the unit cells from 9 to 12 are with identical resonators and the rest are made of different resonators. With this distribution, the cavity heights are further optimized by the boundary integral method using the objective function equation (2), in which the intercell coupling is considered.

To test the design parameters by the boundary integral method, we use the COMSOL Multiphysics software to simulate the performance of achromatic focusing by choosing the length of unit cell as $\Lambda = 2.45$ cm. The simulated scattered amplitude along the axis of metalens ($x = 0$ cm) is plotted in figure 4(a) for a normally incident plane wave of unit amplitude without considering the viscous friction due to the existence of narrow channels. It is observed that, in the range from 2800 to 5600 Hz, the scattered amplitude at the focal point for the high frequency part is larger than that for the low frequency part due to a fixed size of metalens. And owing to the reflected phase shown in figure 3(b), which does not perfectly satisfy equation (1), the scattered amplitude at the focal point in figure 4(a) shows a slight fluctuation with frequency. Note that for the frequency lower than 2800 Hz, although acoustic focusing can still be obtained, the focusing position moves slowly toward the metalens, whereas for frequency higher than 5600 Hz, the reflected acoustic field becomes complex and the unwanted side-lobes appear in the zone of focusing. For comparison, when the effect of the viscous friction is considered, although the maximum scattered amplitude is reduced, the viscous friction has a neglected effect on the focusing position as shown in figure 4(b). Note that the following simulated results are obtained by considering the effect of the viscous friction. In addition, figure 5 gives the scattered amplitude $|p_s(x,\ z)|$ for a plane wave normally incident on the metalens at four frequencies, and sound energy is focused at the predetermined focusing position, except for a slight shift in the focus position at low frequency.

Although the achromatic reflected metalens is designed under normal incidence of plane waves, it works well for focusing the acoustic field of a point source. The simulated scattered amplitude along the axis of metalens ($x = 0$ cm) is plotted in figure 6(a) for a point source at position (0, −217 cm). In order to compare with the results obtained under normal incidence of plane waves, the incident amplitude of a point source at the center of metalens is normalized to unity. By comparing figures 4(a) and 6(a), it is found that the focal length for the incidence of a point source is larger than that of plane wave. This is because that the point source is located in the near-field zone, $L^2/\lambda > 217$ cm, where $L \approx 59$ cm is the aperture of the lens. Figure 6(b) give the frequency dependence of scattered amplitude along a line, which passes through the focal point and is perpendicular to the axis.

Then an experiment is carried out to confirm the theoretical predict. Figure 3(a) shows a metalens of 24 unit cells and of thickness 4 cm (along the z-axis), which is fabricated by 3D printing. Note that two walls perpendicular to the y-axis are added to the metalens and their thickness is 2 mm. The metalens is sandwiched in between two Plexiglas plates of dimensions 3 m × 2 m × 8 mm, the edge of which is closed by anechoic walls. A loudspeaker is placed at a distance 217 cm from the metalens to radiates eight cycles of sine waves in the frequency range from 2800 to 5600 Hz. A probe microphone is moved in 5mm step by a stepping motor to

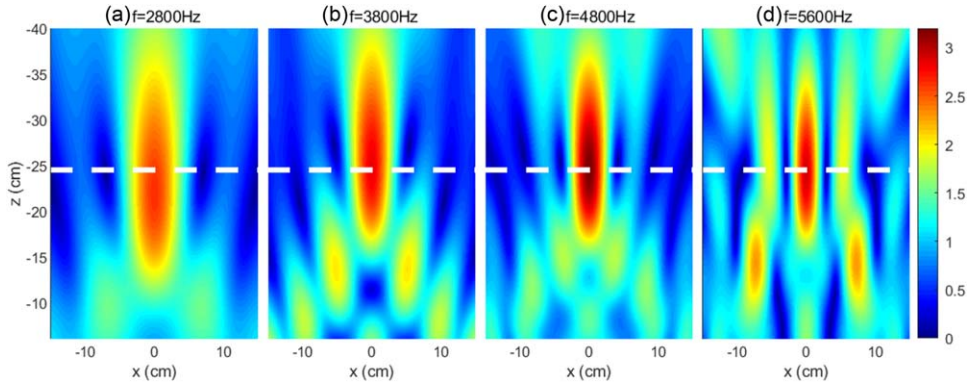

Figure 5. The scattered amplitude $|p_s(x, z)|$ for a plane wave of unit amplitude normally incident on the metalens at four frequencies, (a) $f = 2800$ Hz, (b) $f = 3800$ Hz, (c) $f = 4800$ Hz, and (d) $f = 5600$ Hz. Note that dashed lines represent predetermined focusing positions, where the focal length is $f_0 = 10\Lambda = 24.5$ cm.

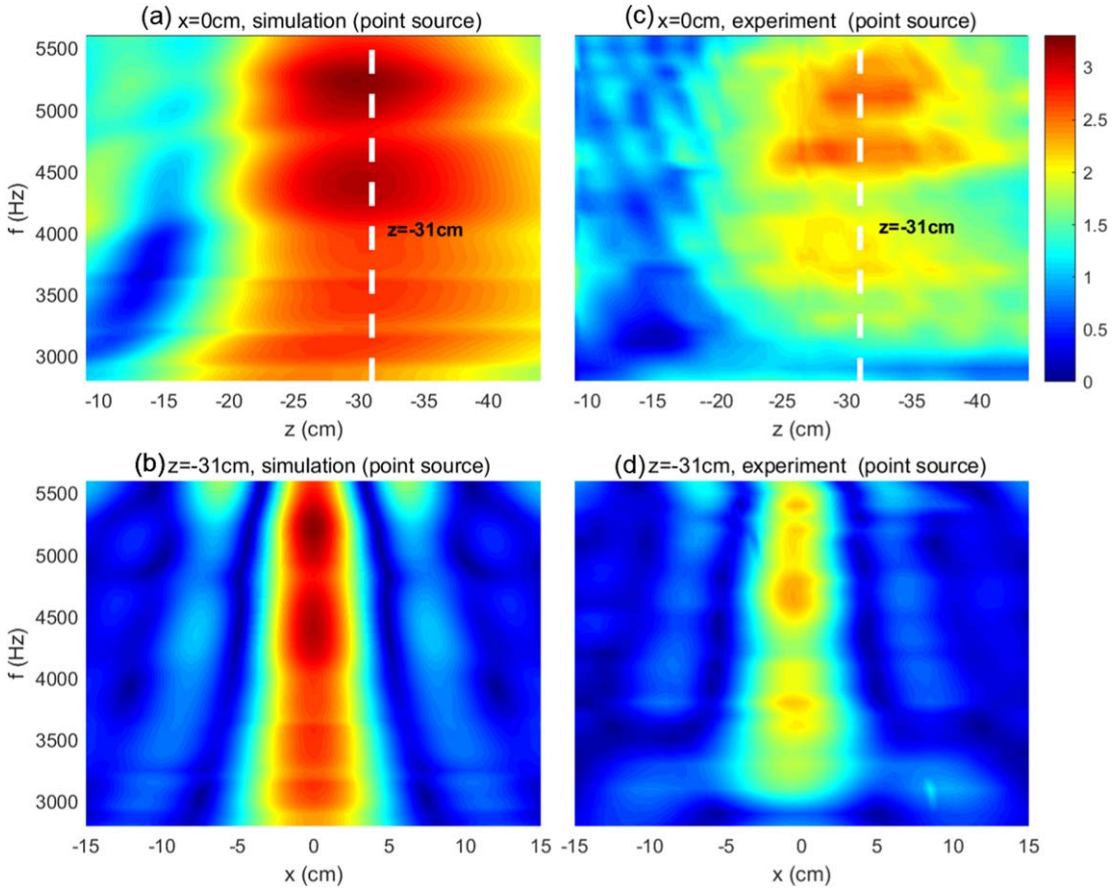

Figure 6. Frequency dependence of scattered amplitude $|p_s(x, z)|$ along $x = 0$ cm, and $z = -31$ cm. Simulated results in (a) and (b) are obtained for a point source located at position $(0, -217$ cm), where the focusing position is $(0, -31$ cm), and the corresponding experimental results are given in (c) and (d). Note that the incident amplitude of a point source at the center of metalens is normalized to unity.

detect acoustic field along two measurement lines marked in figure 3(a). All the receiving acoustic signals are achieved by the National Instruments PXI-6733 and PXI-4496. By the subtraction of sound pressure being measured with and without the aid of acoustic metalens, Figure 6(c) and (d) give the experimental scattered amplitude, which are consistent with theoretical predictions.

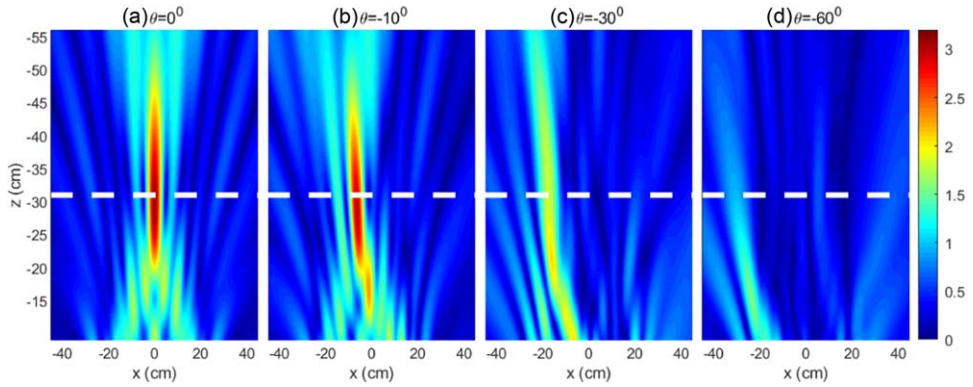

Figure 7. The scattered amplitude $|p_s(x, z)|$ at frequency $f = 4400$ Hz when a source is located at four different azimuth angles θ with respect to the center of metalens, (a) $\theta = 0^0$, (b) $\theta = -10^0$, (c) $\theta = -30^0$, and (d) $\theta = -60^0$. Note that the dashed lines represent predetermined focusing positions, where the focal length is $f_0 = 31$ cm.

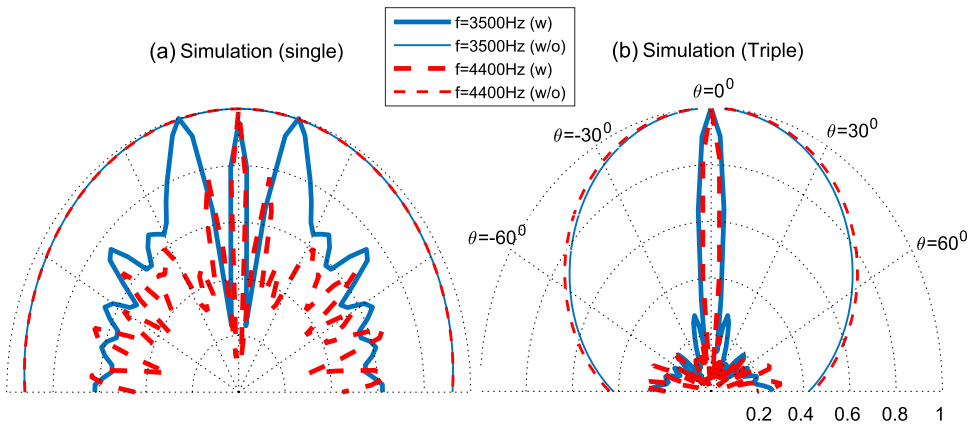

Figure 8. (a) Simulated beampatterns obtained by a single sensor with and without the aid of metalens at two frequencies, whereas (b) for simulated beampatterns obtained using triple sensors separated by a subwavelength interval. Note that the sensors are located near the focal point of reflected metalens.

4. Highly directional and long-distance acoustic probing scheme

In this section, a highly directional and long-distance acoustic probing scheme is proposed by a combination of an achromatic reflected metalens and triple sensors separated by a subwavelength interval, and its performance is tested by an experiment.

Usually, when a sensor is located at the focal point position of reflected metalens, the received signals are enhanced, resulting in a long-distance probing. In addition, the focal point position is also sensitive to the angles of incident waves. The scattered amplitudes at four different azimuth angles in figure 7 are obtained when a source is located at a distance 217 cm from the center of metalens, where the incident amplitude at the center of metalens is normalized to unity. It is shown that the scattered amplitude is high at the predetermined focusing position for the normal incidence, and the position of the maximum scattered amplitude deviates from the predetermined focusing position when the incident angle deviates from the normal, leading to a decrement of the scattered amplitude at the predetermined focusing position, which provides a possibility to design a highly directional acoustic sensor. Figure 8(a) shows the simulated beampatterns of an omnidirectional sensor at the focal point with and without the aid of achromatic reflected metalens. Owing to the interferences between the incident waves and reflected waves, the beampatterns vary with frequency for a sensor with the aid of reflected metalens, leading to a degraded directional performance. In order to eliminate these interferences, a signal processing method is proposed by using triple sensors, which are located near the focal point, at positions $z_1 = -f_0 - \Delta/2, z_2 = -f_0$, and $z_3 = -f_0 + \Delta/2$ (see in figure 3(a)), and the corresponding pressures are denoted as p_1, p_2 and p_3, respectively. We assume a unit plane wave, $p = \exp(ik \sin\theta x + ik \cos\theta z)$, where θ is defined as the angle with respect to the z-axis in figure 1(a), $-\pi/2 < \theta < \pi/2$ for an incident wave and $\pi/2 < |\theta| < \pi$ for a reflected wave. Owing to the subwavelength interval between neighbouring sensors,

$k\Delta/2 \ll 1$, Taylor expansion approximation is adopted to obtain an output quantity $\tilde{p}_2$

$$\tilde{p}_2 \equiv p_2 + \frac{p_1 - p_3}{jk\Delta} \approx (1 - \cos\theta)\exp^{-jk\cos\theta f_0} = (1 - \cos\theta)p_2. \tag{3}$$

It is seen from equation (3) that the output amplitude of $\tilde{p}_2$ is higher than that of p_2 for a reflected wave ($\pi/2 < |\theta| < \pi$), however, for an incident wave ($|\theta| < \pi/2$), the output amplitude of $\tilde{p}_2$ is smaller than that of p_2, and the incident wave is totally removed from $\tilde{p}_2$ at angle $\theta = 0$. Owing to the linearity of equation (3), it can be applied to eliminate incident waves when the total sound field consists of incident waves and reflected waves, we then define a beampattern for triple sensors with the aid of achromatic reflected metalens as

$$D(\theta) = \frac{\left| p_2 + \frac{p_1 - p_3}{jk\Delta} \right|}{\max\left(\left| p_2 + \frac{p_1 - p_3}{jk\Delta} \right| \right)}, \tag{4}$$

where $D(\theta)$ represents the relative amplitude of reflected waves at the focal point for an incident wave at angle θ. Figure 8(b) shows the simulated beampatterns obtained by triple sensors with and without the aid of achromatic reflected metalens, where the simulated beampatterns without the reflected metalens are obtained by $\tilde{D}(\theta) = \dfrac{\left| p_2 - \frac{p_1 - p_3}{jk\Delta} \right|}{\max\left(\left| p_2 - \frac{p_1 - p_3}{jk\Delta} \right| \right)}$. It is then concluded from figures 8(a) and (b) that a highly directional beampattern (the mainlobe width about 8^0) is achieved by a combination of a signal processing method (equation (4)) and an achromatic reflected metalens. Note that a point source is located at a distance of 217 cm away from the origin, and the positions of triple sensors are determined by choosing $f_0 = 31$ cm due to the experimental result in figure 6(c).

An experiment is carried out to test the performance of highly directional acoustic probing. By moving a loudspeaker along a circle of radius 217 cm, which is centered at origin, seven nominal incident angles, $\theta = 0^0$, $\theta = \pm 5^0$, $\theta = \pm\ 10^0$, $\theta = \pm\ 15^0$, are chosen according to the dimensions of the waveguide. Three sensors are located at positions marked in figure 3(a), where $f_0 = 31$ cm is chosen according to the experimental result in figure 6(c). Figures 9(c) and (d) give experimental measurements of beampatterns with the aid of achromatic reflected metalens in the frequency range from 2800 to 5600 Hz. For a single sensor, owing to the interferences between the incident waves and reflected waves, the measured beampatterns are not uniform with frequency, which is consistent with the numerical simulation in figure 9(a), however, for triple sensors, the interferences are eliminated by equation (4), resulting in a highly directional beampattern, which is also confirmed by the numerical simulation in figure 9(b). Note that when a source is located in the far-field zone, i.e. $r_d \gg L^2/\lambda$ (r_d, a distance between the point source and achromatic reflected lens), the triple sensors should be located near the focal point ($f_0 = 24.5$ cm).

5. Conclusion

In conclusion, an achromatic reflected metalens is developed based on hybrid resonance and anti-resonance induced by couplings between two Helmholtz resonators, where the anti-resonance plays a role in reducing the thickness of metalens. Theoretical and experimental results demonstrates that the position of focal point has a very weak frequency dependence over a broadband. Different from the application of achromatic metalens for full-color camera in optics [2–5], here a highly directional and long-distance acoustic probing scheme is proposed by a combination of achromatic reflected metalens and triple sensors separated by a subwavelength interval, in which a signal processing method is presented to eliminate the interferences between incident waves and reflected waves, resulting in a highly directional beampattern confirmed by an experiment. Although no interference exists between incident waves and transmitted waves for an achromatic transmitted lens, an achromatic reflected lens has advantages in focusing efficiency and bandwidth, which is a good choice for a long-distance acoustic probing. Note that when the physical size of sensor is normalized by the operating wavelength, our designed directive sensor is competitive with respect to the directive transducer in the market, such as Simrad ES 70-11 of beamwidth 11^0 and Simrad ES70-7C of beamwidth 7^0, which are the 70 kHz split beam echo sounder transducers in water. Since the reflected metalens plays a role in focusing acoustic waves, the main advantage of our design is that a highly directional acoustic probing can be achieved with a much smaller number of piezoceramic elements than that adopted by the directive transducer in market, which is very attractive in low frequency underwater acoustic probing.

On one hand, our result has demonstrated that anti-resonance provides an extra degree of freedom to control local phases of reflected waves, which can be used for wavefront manipulation, such as the metasurface

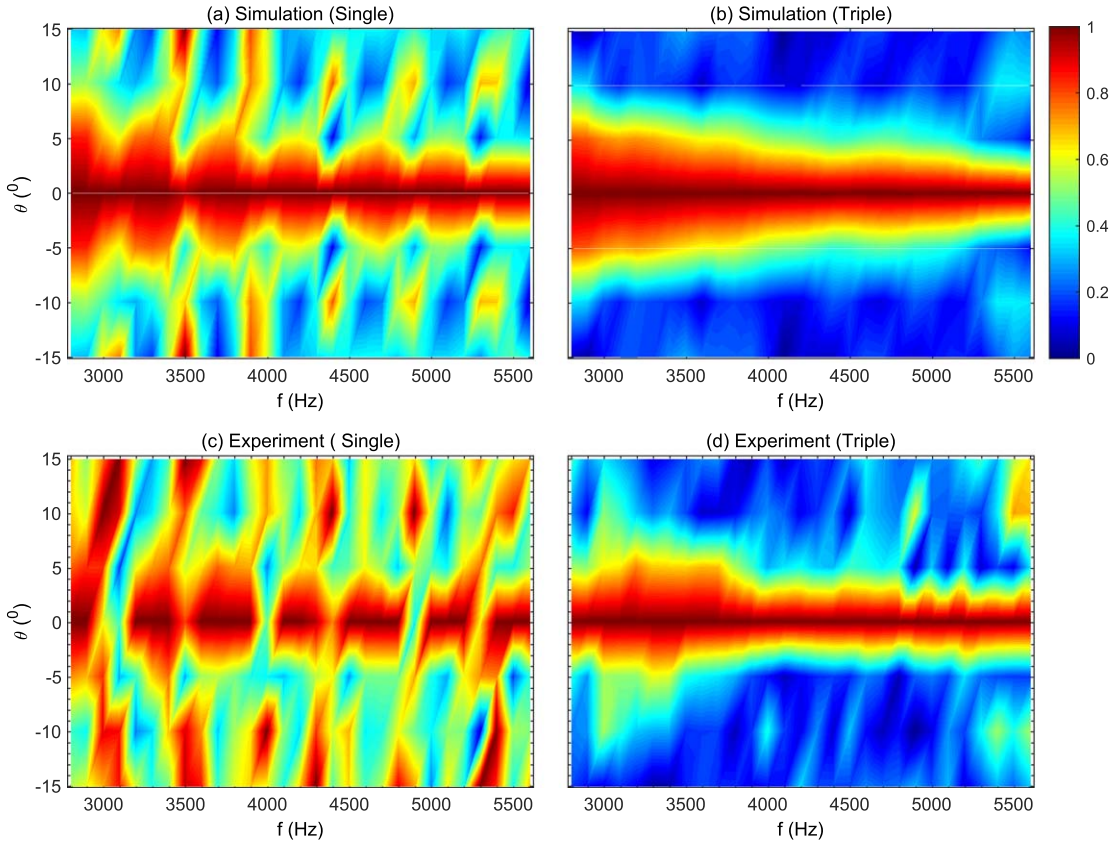

Figure 9. With the aid of achromatic reflected metalens, (a) and (b) are for the simulated beampatterns by a single sensor and triple sensors, respectively, whereas (c) and (d) are for experimental measurements.

carpet cloaking [43]. On the other hand, the highly directional acoustic probing scheme can be extended to design a highly directional monostatic transducer at a low cost, which may find its application in underwater warning.

Acknowledgments

We wish to acknowledge the support of the National Science Foundation of China under Grant No. 11674293.

Appendix A. Derivation of reflection coefficient

We assume a unit incident sound pressure, $p_{\text{inc}} = \exp(\mathrm{i}k\sin\theta x + \mathrm{i}k\cos\theta z)$, where θ is defined as the angle of incidence with respect to the z-axis in figure 1(a). According to Floquet's theory, sound fields on the side ($z < 0$) can be expanded in series, $p_r = \sum_n r_n \mathrm{e}^{\mathrm{i}k\beta_n x + k\alpha_n z}$, where r_n being the reflection coefficient of the nth diffraction order with the horizontal wavenumber $k\beta_n = k\sin\theta + 2\pi n/\Lambda$, and the vertical wavenumber $\mathrm{i}k\alpha_n = k\sqrt{1-\beta_n^2}$, for $n = 0, \pm 1, \pm 2, \cdots$. Since the working frequency is much lower than the cutoff, the plane wave approximation is used for the waves in the inlet of Helmholtz resonator. By introducing volume velocities $U_1(0)$ and $U_2(0)$ at positions $x_1 = -\Lambda/4$ and $x_2 = \Lambda/4$, in which x_1 and x_2 denote the inlets of Helmholtz resonators A and B, respectively. We then obtain from the continuity of normal velocity at boundary $z = 0$

$$r_n = \delta_{0n} - (i\alpha_n)^{-1}\Phi_{1n}(\theta)R_\Sigma U_1(0) - (i\alpha_n)^{-1}\Phi_{2n}(\theta)R_\Sigma U_2(0), \tag{A1}$$

where $R_\Sigma = \rho c/\Lambda$, $\Phi_{1n}(\theta) = b^{-1}\int_{x_1-b/2}^{x_1+b/2}\exp(-\mathrm{i}k\beta_n x)\mathrm{d}x$, and $\Phi_{2n}(\theta) = b^{-1}\int_{x_2-b/2}^{x_2+b/2}\exp(-\mathrm{i}k\beta_n x)\mathrm{d}x$. By introducing an average pressure $\bar{p}_1(0)$ and $\bar{p}_2(0)$ at positions $x_1 = -\Lambda/4$ and $x_2 = \Lambda/4$, respectively, we obtain

from the continuity of sound pressure at boundary $z = 0$

$$2\Phi_{10}^{*}(\theta) = (Z_{11} + Z_1)\,U_1(0) + Z_{12}\,U_2(0), \tag{A2}$$

$$2\Phi_{20}^{*}(\theta) = Z_{21}\,U_1(0) + (Z_{22} + Z_2)\,U_2(0), \tag{A3}$$

where Z_1 and Z_2 are acoustic impedances of Helmholtz resonators A and B, respectively. And the other physical quantities $Z_{11} = \sum_n (i\alpha_n)^{-1}|\Phi_{1n}(\theta)|^2 R_\Sigma$, $Z_{12} = \sum_n (i\alpha_n)^{-1}\Phi_{1n}^{*}(\theta)\Phi_{2n}(\theta)R_\Sigma$, $Z_{21} = \sum_n (i\alpha_n)^{-1}\Phi_{2n}^{*}(\theta)\Phi_{1n}(\theta)R_\Sigma$, and $Z_{22} = Z_{11}$ represent couplings among Helmholtz resonators. By substituting $U_1(0)$ and $U_2(0)$ (the solution of equation (A2) and equation (A3)) into equation (A1), we get the reflection coefficient r_0 at incident angle $\theta = 0$, from which the local phase ϕ of reflected waves can be extracted. Note that the reflection r_0 obtained at the large incident angle is not very accurate, especially when the averages of normal velocity and pressure over the inlet become invalid at high frequency.

Appendix B. Anti-resonance and hybrid resonance

For a sound wave normally incident on a metasurface, with each unit cell being constructed by a combination of two different resonators A and B, it is found that the value of reflection coefficient r_0 in equation (A1) is 1 if the total volume velocity over a unit cell is zero, i.e. $U_1(0) + U_2(0) = 0$, which is consistent with the definition of anti-resonance. Then, by letting $r_0 = 1$, i.e. the local phase ϕ is zero (or 2π), we obtain a condition of anti-resonance

$$Z_2 + Z_1 + i\,\mathrm{Im}\,(2Z_{11} - 2Z_{12}) = 0, \tag{B1}$$

where Im() denotes the imaginary part. If couplings among Helmholtz resonators are neglected, then equation (B1) is simplified as

$$Z_2 + Z_1 = 0, \tag{B2}$$

From which we know that anti-resonance occurs between two different resonances [29]. In addition, equation (B2) is consistent with the condition of acoustic transparency investigated in [38–40]. Note that for two identical Helmholtz resonators ($Z_1 = Z_2$), only if acoustic impedance $Z_1 = \infty$, then $r_0 = 1$ is satisfied with $U_1(0) = U_2(0) = 0$.

It is well known that hybrid resonance occurs when an effective acoustic impedance over a unit cell is zero, resulting $r_0 = -1$. A condition of hybrid resonance is obtained

$$(i\,\mathrm{Im}\,(Z_{11}) + Z_1)(i\,\mathrm{Im}\,(Z_{11}) + Z_2) - (i\,\mathrm{Im}\,(Z_{12}))^2 = 0. \tag{B3}$$

If two resonant frequencies of resonators A and B are far away from each other, for example, $|Z_2| \gg |Z_1| \approx 0$ (near resonance of resonator A), equation (B3) can be simplified as, $i\,\mathrm{Im}\,(Z_{11}) + Z_1 = 0$, which means the frequency of hybrid resonance is mainly determined by resonator A.

Appendix C. Scattered sound field from a reflected metalens predicted by the boundary integral method

In order to consider the couplings among different cells, a boundary integral method is introduced. Using Green's theorem, total pressure on the side ($z < 0$) is

$$p(\vec{r}) = p_{\mathrm{inc}} + \int G(\vec{r},\,\vec{r}\,')\frac{\partial p(\vec{r}\,')}{\partial z'}|_{z'=0} - \frac{\partial G(\vec{r},\,\vec{r}\,')}{\partial z'}p(\vec{r}\,')|_{z'=0}\mathrm{d}x', \tag{C1}$$

where $G(\vec{r},\,\vec{r}\,') = \dfrac{i}{4}H_0^{(1)}(k\sqrt{(x-x')^2 + (z-z')^2})$ denotes the Green's function for the two-dimensional Helmholtz equation in free space, and the integral is over the surface of reflected metalens. Using the equation of motion $ik\rho_0 c_0 u_z = \partial p(\vec{r})/\partial z$ and the definition of specific normal acoustic impedance $Z_s(x) = p/u_z$ at boundary $z = 0$, equation (C1) is rewritten as

$$p(\vec{r}) = p_{\mathrm{inc}} + \int G(\vec{r},\,\vec{r}\,')\frac{ik\rho_0 c_0}{Z_s(x')}p(\vec{r}\,')|_{z'=0} - \frac{\partial G(\vec{r},\,\vec{r}\,')}{\partial z'}p(\vec{r}\,')|_{z'=0}\mathrm{d}x'. \tag{C2}$$

For x' at rigid wall, $Z_s = \infty$, whereas for x' located at the inlet of Helmholtz resonator, Z_s is expressed as, $Z_s = aZ_H$, in which a is the size of throat and Z_H represents the acoustic impedance of Helmholtz resonator. By discretizing the integral equation (C2), total sound pressure $p(\vec{r}\,')$ at the surface of metalens can first be obtained, and then the scattered pressure $p_s(\vec{r}) = p(\vec{r}) - p_{\mathrm{inc}}$ at an arbitrary position ($z < 0$) can be calculated.

References

[1] Pendry J B 2000 Negative refraction makes a perfect lens *Phys. Rev. Lett.* **85** 3966–9

[2] Wang S *et al* 2017 Broadband achromatic optical metasurface devices *Nat. Commun.* **8** 187
[3] Shrestha S, Overvig A C, Lu M, Stein A and Yu N 2018 Broadband achromatic dielectric metalenses *Light: Sci. Appl.* **7** 85
[4] Wang S *et al* 2018 A broadband achromatic metalens in the visible *Nat. Nanotechnol.* **13** 227–32
[5] Lin R J *et al* 2019 Achromatic metalens array for full-colour light-field imaging *Nat. Nanotechnol.* **14** 227–31
[6] Climente A, Torrent D and Sanchez-Dehesa J 2010 Sound focusing by gradient index sonic lenses *Appl. Phys. Lett.* **97** 104103
[7] Martin T P, Nicholas M, Orris G J, Cai L-W, Torrent D and Snchez-Dehesa J 2010 Sonic gradient index lens for aqueous applications *Appl. Phys. Lett.* **97** 113503
[8] Zigoneanu L, Popa B-I and Cummer S A 2011 Design and measurements of a broadband two-dimensional acoustic lens *Phys. Rev.* B **84** 024305
[9] Liang Z and Li J 2012 Extreme acoustic metamaterial by coiling up space *Phys. Rev. Lett.* **108** 114301
[10] Li Y, Liang B, Tao X, Zhu X F, Zou X Y and Cheng J C 2012 Acoustic focusing by coiling up space *Appl. Phys. Lett.* **101** 233508
[11] Li Y, Yu G, Liang B, Zou X, Li G, Cheng S and Cheng J 2014 Three-dimensional ultrathin planar lenses by acoustic metamaterials *Sci. Rep.* **4** 6830
[12] Romero-García V, Cebrecos A, Picó R, Sánchez-Morcillo V J, Garcia-Raffi L M and Sánchez-Pérez J V 2013 Wave focusing using symmetry matching in axisymmetric acoustic gradient index lenses *Appl. Phys. Lett.* **103** 264106
[13] Park C M and Lee S H 2015 An acoustic lens built with a low dispersion metamaterial *J. Appl. Phys.* **117** 034904
[14] Park C M, Kim C H, Park H T and Lee S H 2016 Acoustic gradient-index lens using orifice-type metamaterial unit cells *Appl. Phys. Lett.* **108** 124101
[15] Moleron M, Serra-Garcia M and Daraio C 2014 Acoustic Fresnel lenses with extraordinary transmission *Appl. Phys. Lett.* **105** 114109
[16] Calvo D C, Thangawng A L, Nicholas M and Layman C N 2015 Thin Fresnel zone plate lenses for focusing underwater sound *Appl. Phys. Lett.* **107** 014103
[17] Jiménez N, Romero-García V, Picó R, Cebrecos A, Sánchez-Morcillo V J, Garcia-Raffi L M, Sánchez-Pérez J V and Staliunas K 2014 Acoustic Bessel-like beam formation by an axisymmetric grating *Europhys. Lett.* **106** 24005
[18] Jiménez N, Romero-García V, Picó R, Garcia-Raffi L M and Staliunas K 2015 Nonlinear focusing of ultrasonic waves by an axisymmetric diffraction grating embedded in water *Appl. Phys. Lett.* **107** 304103
[19] Wang W, Xie Y, Konneker A, Popa B and Cummer S A 2014 Design and demonstration of broadband thin planar diffractive acoustic lenses *Appl. Phys. Lett.* **105** 101904
[20] Hyun J, Kim Y T, Doh I, Ahn B, Baik K and Kim S H 2018 Realization of an ultrathin acoustic lens for subwavelength focusing in the megasonic range *Sci. Rep.* **8** 9131
[21] Chen J, Xiao J, Lisevych D, Shakouri A and Fan Z 2018 Deep-subwavelength control of acoustic waves in an ultra-compact metasurface lens *Nat. Commun.* **9** 4920
[22] Chen J, Rao J, Lisevych D and Fan Z 2019 Broadband ultrasonic focusing in water with an ultra-compact metasurface lens *Appl. Phys. Lett.* **114** 104101
[23] Zhu Y F, Zou X Y, Li R Q, Jiang X, Tu J, Liang B and Cheng J C 2015 Dispersionless manipulation of reflected acoustic wavefront by subwavelength corrugated surface *Sci. Rep.* **5** 10966
[24] Wu X, Xia X, Tian J, Liu Z and Wen W 2016 Broadband reflective metasurface for focusing underwater ultrasonic waves with linearly tunable focal length *Appl. Phys. Lett.* **108** 163502
[25] Fan X D, Zhu Y F, Liang B, Yang J, Yin L L, Yang J and Cheng J C 2016 Three-dimensional ultra-broadband focusing flat mirror for airborne sound *Appl. Phys. Lett.* **109** 153501
[26] Amin M, Siddiqui O, Farhat M and Khelif A 2018 A perfect Fresnel acoustic reflector implemented by a Fano-resonant metascreen *J. Appl. Phys.* **123** 144502
[27] Amin M, Siddiqui O, Orfali W, Farhat M and Khelif A 2018 Resonant beam steering and carpet cloaking using an acoustic transformational metascreen *Phys. Rev. Appl.* **10** 064030
[28] Qi S and Assouar B 2018 Ultrathin acoustic metasurfaces for reflective wave focusing *J. Appl. Phys.* **123** 234501
[29] Ma G, Yang M, Xiao S, Yang Z and Sheng P 2014 Acoustic metasurface with hybrid resonances *Nat. Mater.* **13** 873
[30] Merkel A, Theocharis G, Richoux O, Romero-Garca V and Pagneux V 2015 Control of acoustic absorption in one-dimensional scattering by resonant scatterers *Appl. Phys. Lett.* **107** 244102
[31] Li J, Wang W, Xie Y, Popa B and Cummer S A 2016 A sound absorbing metasurface with coupled resonators *Appl. Phys. Lett.* **109** 091908
[32] Fu C, Zhang X, Yang M, Xiao S and Yang Z 2017 Hybrid membrane resonators for multiple frequency asymmetric absorption and reflection in large waveguide *Appl. Phys. Lett.* **110** 021901
[33] Ryoo H and Jeon W 2018 Perfect sound absorption of ultra-thin metasurface based on hybrid resonance and space-coiling *Appl. Phys. Lett.* **113** 121903
[34] Liu G S, Peng Y Y, Liu M H, Zou X Y and Cheng J C 2018 Broadband acoustic energy harvesting metasurface with coupled Helmholtz resonators *Appl. Phys. Lett.* **113** 153503
[35] Dong Y, Yu G, Wang X, Niu X, Wu K and Wang N 2017 Broadband and wide-angle blazed acoustic gratings using multiple coupled Helmholtz resonators *Appl. Phys. Express.* **10** 097201
[36] Yang Z, Mei J, Yang M, Chan N H and Sheng P 2008 Membrane-type acoustic metamaterial with negative dynamic mass *Phys. Rev. Lett.* **101** 204301
[37] Sui N, Yan X, Huang T Y, Xu J, Yuan F G and Jing Y 2015 A lightweight yet sound-proof honeycomb acoustic metamaterial *Appl. Phys. Lett.* **106** 171905
[38] Santillan A and Bozhevolnyi S I 2011 Acoustic transparency and slow sound using detuned acoustic resonators *Phys. Rev.* B **84** 064304
[39] Yu G and Wang X 2014 Acoustical 'transparency' induced by local resonance in Bragg bandgaps *J. Appl. Phys.* **115** 044913
[40] Qi L, Yu G, Wang X, Wang G and Wang N 2014 Interference-induced angle-independent acoustical transparency *J. Appl. Phys.* **116** 234506
[41] Li Y *et al* 2019 Reflection phase dispersion editing generates wideband invisible acoustic Huygens's metasurface *J. Acoust. Soc. Am.* **146** 166–71
[42] Ma C, Gao S, Cheng Y and Liu X 2019 Acoustic metamaterial antennas for combined highly directive-sensitive detection *Appl. Phys. Lett.* **115** 053501
[43] Faure C, Richoux O, Félix S and Pagneux V 2016 Experiments on metasurface carpet cloaking for audible acoustics *Appl.Phys. Lett.* **108** 064103